Numerical modelling of the transition from a closed wall film to discrete liquid rivulets

Adrian Seck*, Bernhard Weigand†
*†University of Stuttgart, Institut for Aerospace Thermodynamics, 70569 Stuttgart, Germany
*Corresponding author: adrian.seck@itlr.uni-stuttgart.de

Abstract
Fogging systems are often used in stationary gas turbines as they offer a cheap, easy, and very adjustable method to increase a turbine's power output. With high-fogging, water droplets enter the compressor cascade, where they evaporate and continuously cool down the air throughout the compression. Depending on the spray characteristics and droplet interactions, various droplet sizes can occur. Due to inertia, only small droplets with diameter $d < 10\mu m$ are able to follow the surrounding air flow. Larger droplets are likely to hit the compressor blades or casing, where they interact with the component. A distinct part of the impacting droplet deposits on the surface and a wall film develops. Experiments have shown that the wall film on the suction side of a compressor blade splits up into liquid rivulets.
Within the current study an adaption to the numerical wall film formulation is developed to enable the transition from a closed wall film to discrete liquid rivulets. The adaption also allows the propagation of the ligaments due to surrounding conditions, may it be an air flow, or volume forces. The core of the adaption is a new treatment of the surface tension, as it distinguishes between cells with and without a contact line. This results in one main advantage: liquid rivulets can emerge from a closed film, but coalescence of different rivulets is also possible.
Besides single liquid rivulets under varying conditions of the surrounding flow, mainly the applicability to liquid flows over an inclined plate has been investigated. Here, cases with and without external air flow have been simulated. Finally, the application case of a compressor blade of a staggered grid under high-fogging conditions has been simulated. The transition point can be evaluated and compared with experimental data.

Keywords
High-fogging, surface tension modeling, wall film break up, liquid rivulets

Introduction

Today, the high-fogging technique is widely used in industrial gas turbines to rapidly increase it's power output. This offers the possibility to overcome fluctuations in the power grid. The numerical description of droplets entering the compressor has already been focussed by the authors in the past. In Gomaa [3] a routine, using the Euler-Lagrange formulation, is introduced to simulate the trajectories of the droplets. Also, the breakup of droplets due to strong gas shear is included. Additionally, the general framework for the simulation of a liquid wall film on a curved surface is given by the Navier-Stokes equations simplified in analogy to the lubrication theory. Further description of the equations will follow later. Gomaa and Weigand [4] numerically investigated the impact of single droplets on thin wall films. From this, an empirical model to predict the outcome of droplet splashing is evaluated. The model is used to calculate the resulting mass and momentum of droplets impacting on wetted surfaces, which contribute to the movement of the liquid film. To consider the main process of high-fogging, the evaporation of droplets, an extensive parameter study has been performed numerically. Direct numerical simulations of droplets were used to evaluate the evaporation rate under varying flow conditions, resulting in a simple correlation [10]. Within the present paper, the focus lies on the detailed description of the liquid film on the surface. The deposition of liquid on the compressor blades results in a thin film, which covers the blade surface. Due to the surrounding gas flow and the impacting droplets, shear stresses act on the film and carry it towards the trailing edge. However, experimental investigations have shown that the liquid film breaks up into separate liquid rivulets. So far, our numerical model is only capable to simulate closed films. Therefore, the scope of this paper is to introduce a numerical model, which can reproduce the liquid rivulets and their movement due to the prevailing conditions. First, a short review of the treatment of liquid films and rivulets in literature is given, followed by the mathematical description of thin films. The next section treats the adaption of the model to account for rivulet flow. The final section shows results for the adapted mathematical model.

Fundamentals of liquid films and rivulets

The insight into the details of liquid film or rivulet flow is of interest for many engineering applications. In literature, the appearance in nuclear reactors, airplanes in heavy rain, and high-fogging is often mentioned. Although there exists a common interest in the development of the wall film and in the major question whether the film will break up into separated rivulets, there is also an important difference in the physical processes. On one hand, there are falling films on inclined surfaces, which are only driven by gravity, and on the other hand, there are shear driven films, where the liquid flow is forced by a surrounding gas flow. For the latter, the existence of impacting droplets onto the liquid film is also of importance for the stability of the film. So far, many authors regarded this topic analytically, all having the same goal to state a minimum film thickness for which the film is stable and no breakup occurs. The

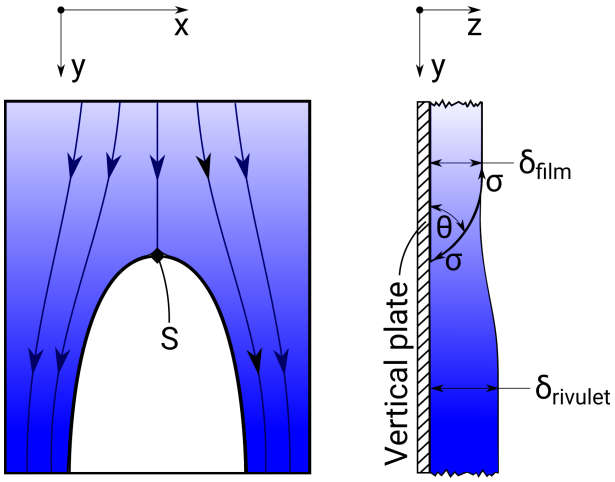

Figure 1. Dry patch formation in liquid layer on a vertical plate. Plan view on left side, with stagnation point S and approximate stream lines. Cross-section in flow direction through S with geometrical information about liquid heights δ_{film} and $\delta_{rivulet}$, surface tension σ and contact angle θ. [5]

preferred method to evaluate this value is mostly a force or energy balance between the intact film and the separate rivulets. Hartley and Murgatroyd [5], for example, were interested in the stability of local dry patches. Therefore, they used a force balance at the stagnation point, see fig. 1. To determine the width of a rivulet, they looked for the minimum of total energy over the rivulet cross-section. This procedure has also been used by other authors. To get the total energy, the potential energy, the surface energy, and the kinetic energy need to be determined. The surface energy can be evaluated from the geometry of the rivulet and the three surface tensions, namely the solid-gas σ_{sg}, the liquid-gas σ_{lg} and the liquid-solid σ_{lg}, see fig. 2. For the kinetic energy, the knowledge of the velocity distribution in the rivulet is necessary. Here, the publications differ from each other. While in Hartley and Murgatroyd [5] one dimensional velocity distributions, quadratic for falling rivulets and linear for shear driven rivulets, are used, two dimensional shear driven rivulets are calculated in Al-Khalil et al. [1]. El-Genk and Saber [2] did the same for falling rivulets. So far, all authors assumed the rivulets to be of circular shape. In contrast, Itoh and Matsuno [6] proposed to use a rectangular cross-section and Couette flow for rivulets in strong shear flow. This assumption is not valid for very small liquid flow rates and they adapted the model with a transition from circular to rectangular shape, depending on the flow rate. However, the criteria of minimal film thickness does not result in the correct prediction of the film breakup position. Especially for films with continuous drop impact, this criteria often does not hold, as the drop impact is stabilizing the film. Due to this reason, Al-Khalil et al. [1] stated, that film breakup is not possible in regions with drop impact. To get a valid criteria, Neupert et al. [7] performed a linear stability analysis of the film height. Unfortunately, no definite criteria could be evaluated. Instead, regions of possible breakup are identifiable, which also coincide with the experimental measurements.
In the present study, the authors on one side are interested in the breakup position of a liquid film, but also on the movement of the liquid film and especially of the separated rivulets. However, to the best knowledge of the authors, this has so far only been experimentally investigated in [8] and [13]. Therefore, a numerical tool has been developed to simulate the liquid film flow, as well as the rivulet flow. The procedure will be presented in the next paragraphs.

Numerical treatment of liquid film movement

Following Gomaa [3], the wall film evolution can be described by the Navier-Stokes equations in conservative form. It is assumed that the liquid is an incompressible Newtonian fluid. As the liquid film is very thin, the spatial scales differ substantially in lateral and flow direction. Therefore, the equations can be simplified in analogy to the lubrication theory [9]. Finally, the following equations can be used to evaluate the liquid film motion. For a detailed description

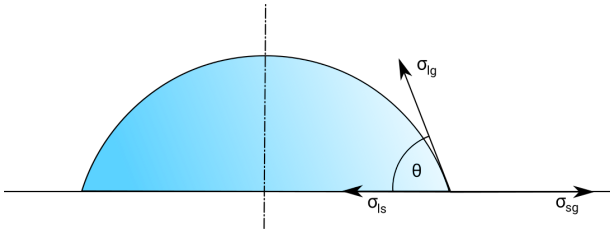

Figure 2. Cross-section of rivulet with contact angle θ and surface tensions σ_{ls}, σ_{lg} and σ_{sg} at the three contact line

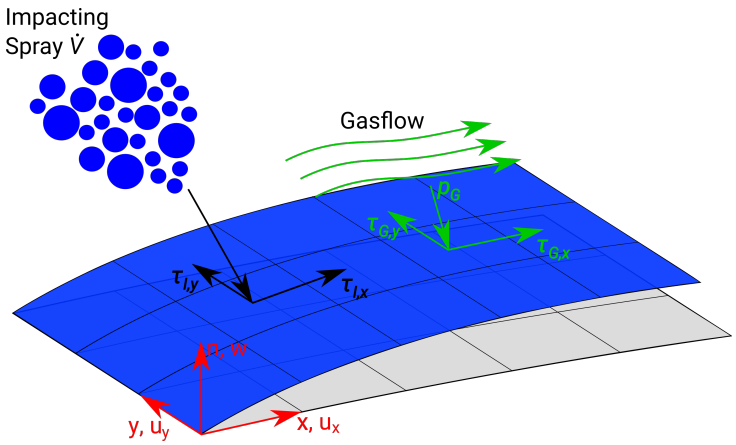

Figure 3. Overview of the important quantities to describe liquid film motion over a surface

of the simplifications, the reader is referred to [3].

$$\nabla_{xy} \cdot \boldsymbol{u_{xy}} + \partial_n w = \dot{h}_I \delta(h - n) \tag{1}$$

$$\rho_L(\partial_t \boldsymbol{u_{xy}} + \nabla \cdot [\boldsymbol{u_{xy}} \boldsymbol{u_{xy}}] + \partial_n [\boldsymbol{u_{xy}} w]) = -\nabla_{xy} \bar{p} + \mu_L \partial_n^2 \boldsymbol{u_{xy}} \tag{2}$$

$$0 = \partial_n \bar{p} \tag{3}$$

For better understanding, fig. 3 shows a schematic view of the main quantities. Equation (1) is the continuity equation, eqs. (2)-(3) are the momentum equation in flow direction x and y, and in lateral direction n, respectively. The subscript xy indicates that the differential operators and vectors are only acting in the x-y-plane.The film velocities are u_{xy} in flow direction, and w in normal direction, $\dot{h}_I$ is the net mass source term that is dissolved into the wall film, h is the film height, and ρ_L and μ_L are the liquid density and dynamic viscosity, respectively. The reduced pressure $\bar{p}$ is defined as the difference between the pressure p and the potential ϕ. All conservative body forces are combined in the potential ϕ, which, in this context, includes the gravitational and centrifugal potential. This leads to $\phi = \rho_L g z - \rho_L(\boldsymbol{\omega} \times r_\perp)/2$, with g being the gravitational acceleration and z the altitude in the inertial system. The boundary conditions for this problem of free surface flow over a wall are given in the following.

$$t = 0: \qquad h = 0 \tag{4}$$

$$n = 0: \qquad \boldsymbol{u_{xy}} = 0 \tag{5}$$

$$n = h: \qquad w = \partial_t h + \boldsymbol{u_{xy}} \cdot \nabla_{xy} h \tag{6}$$

$$n = h: \qquad \bar{p} = p_g - \sigma_{lg}(\kappa + \nabla_{xy}^2 h) - \phi \tag{7}$$

$$n = h: \qquad \mu_L \partial_n \boldsymbol{u_{xy}} = \boldsymbol{\tau_G} + \boldsymbol{\tau_I} \tag{8}$$

Initially, the wall is dry, see eq. (4). Equation (5) states the no slip condition at the interface between liquid and wall. Furthermore, a kinematic boundary condition has to be set, because the shape of the liquid surface is unknown, see eq. (6). Finally, the dynamic boundary conditions (7) and (8) can be derived by considering a force balance along the interface. Here, p_g denotes the gas pressure, σ_{lg} is the surface tension between liquid and gas, κ is the curvature of the wall and τ_G and τ_I are the stresses of gas and spray acting in tangential direction of the film surface, respectively. As the analytical solution of the equations is only possible in some rare special cases, the full solution is obtained numerically.

Adaption of numerical treatment for rivulet flow

The scheme to evaluate the film motion presented above only works for intact films. Although the routine comprises the simulation of three-dimensional conditions, as for example centrifugal forces or strongly three-dimensional flow, the breakup of the film can not be simulated. The reason for this is a missing treatment of the special condition at the three phase contact line. A balance between the different surface tensions, shown in fig. 2, has to be evaluated in x-direction and the influence of the surface tensions needs to be accounted for in the film motion equations. For the intact film, the surface tension between liquid and gas introduces a pressure jump at the surface, depending on the combined curvature of the wall and the liquid surface, as given in eq. (7). In the case of a flat wall κ equals 0, in general $\kappa = \kappa_x + \kappa_y$ holds. For the rivulet flow, this is not applicable at the three phase contact line. Numerically, this leads to the necessity of adapted boundary conditions for cells where a three phase contact line is detected. At

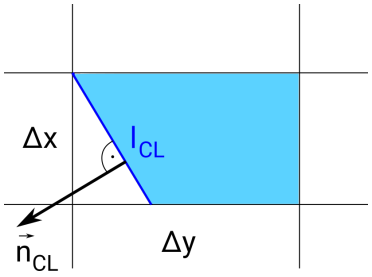

Figure 4. Determination of the length of the contact line l_{CL}

the contact line, the surface tensions, as shown in fig. 2, are in equilibrium, which can mathematically be described by Young's equation [12].

$$\sigma_{sg} = \sigma_{ls} + \sigma_{lg} cos(\theta) \tag{9}$$

With eq. (9) and following [5], the surface tension results in a force at the stagnation point perpendicular to the contact line T_σ, which is given by

$$T_\sigma = \Delta x \cdot \sigma_{lg}(1 - cos(\theta)). \tag{10}$$

Here, Δx is the infinitesimally width of the stagnation point, which in our case can be transferred to the length of the contact line in the cell. The index CL denotes the contact line. The surface tension acting on the intact film is always acting in the wall normal direction, which arises from the thin film assumption. In contrast, T_{CL} is acting tangential to the wall, just like the gas and impacting droplet shear stresses τ_G and τ_I, respectively. For this reason the dynamic boundary condition, eq. (8), is adapted to account for T_σ. To do so, not the resulting force at the contact line is evaluated, but the effect of the surface tension balance at the contact line is casted into a stress term. This can be done by relating the resulting surface tension to the length of the contact line l_{CL}.

$$\tau_{CL} = \sigma_{lg}(1 - cos(\theta)/l_{CL} \tag{11}$$

The adapted dynamic boundary condition then reads

$$n = h: \qquad \mu_L \partial_n \boldsymbol{u_{xy}} = \boldsymbol{\tau_G} + \boldsymbol{\tau_I} + \boldsymbol{\tau_{CL}}. \tag{12}$$

To not account for surface tension twice, the curvature dependent term in eq. (7) is set to zero in cells with a contact line. The length of the contact line has to be estimated based on the film height information. By evaluating the gradient of the wall film height, the normal vector to the contact line can be found. With this, l_{CL} is geometrically evaluated, depending on the cell size, as shown in fig. 4. In general, the contact line length is in the range of $\Delta x, \Delta y \leq l_{CL} \leq \sqrt{\Delta x^2 + \Delta y^2}$.

Numerical results

Within this section, the applicability of the adapted formulation will be shown by comparing the simulation results for a single rivulet flow using the new formulation of the dynamic boundary condition against the old formulation. Different settings will be presented that include a rivulet on an inclined plate, but also a rivulet under the influence of arbitrary shear stress. Afterwards, preliminary results for a liquid film simulation on an inclined plate with breakup, and finally, preliminary results of a calculated film over a compressor blade will be shown.

The first two cases are shown in fig. 5. The setup is an inclined plate under an angle of 70°. The plate has a dimension of $1.2\,\mathrm{m}$ in x- and $0.6\,\mathrm{m}$ in y-direction. At the top ($x = 0\,\mathrm{m}$), a liquid rivulet of width $0.06\,\mathrm{m}$ is initialised at the center of the plate with a volume flow rate of $1.8 \cdot 10^{-6}\,\mathrm{m}^3/\mathrm{s}$. The contact angle between liquid and wall is set to 70°. The colourbar indicates the rivulet height, where darker colours refer to a higher rivulet. The results differ strongly from each other. Figure 5 (left) shows the simulation without a contact line adaption. Therefore, no contact line is detected, no constriction of the rivulet is visible, and it flows down the inclined plate completely undisturbed. In contrast, fig. 5 (right) shows the result with the new dynamic boundary condition. A strong constriction of the initialised rivulet is visible and a narrower rivulet with increased height flows down the plate.

In a second simulation, the behaviour for an existing gas shear stress shall be shown. The used setup is based on the one shown above, except two rivulets are initialised at $x = 0.2\,\mathrm{m}$ and $x = 0.4\,\mathrm{m}$ with a total volume flow of $60 \cdot 10^{-6}\,\mathrm{m}^3/\mathrm{s}$. Additionally, an arbitrary gas shear acts on the rivulets starting from $x > 0.3\,\mathrm{m}$ and it is directed in positive y-direction for $y < 0.3\,\mathrm{m}$ and vice versa for $y > 0.3\,\mathrm{m}$. This setup is chosen to show on one hand, that the rivulet motion is influenced by an existing gas shear, and that two separated rivulets can flow back together. Figure 6 (left) shows the result of the simulation without the adaption. For $x < 0.3\,\mathrm{m}$ the same behaviour as above is visible. The two initialised rivulets flow down the plate, without any constriction or height change. As soon as they reach the region where the gas shear is apparent, they are driven towards the middle and form a unique rivulet, which then flows down to the bottom of the plate. It needs to be mentioned, that the small width and therefore the large height of this rivulet does only arise from the gas shear, which forces the liquid to the middle. Using again the

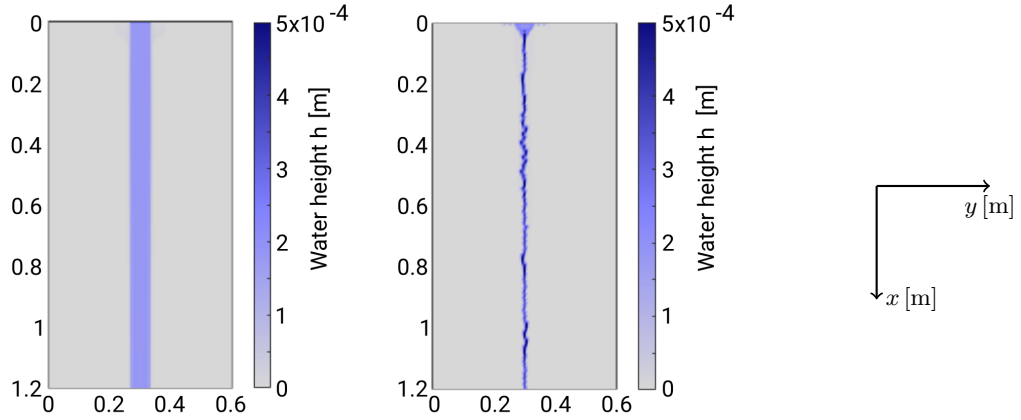

Figure 5. Single rivulet on an inclined surface without (left) and with τ_{CL} (right)

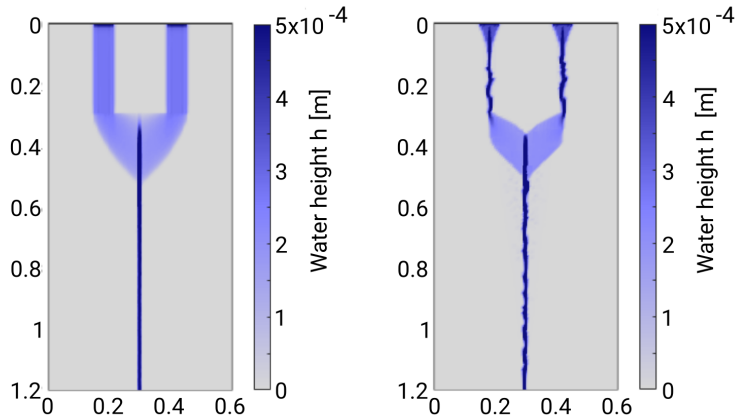

Figure 6. Two rivulets on an inclined surface forced to the middle via τ_G without (left) and with τ_{CL} (right)

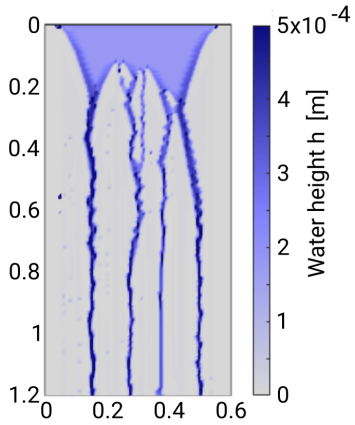

Figure 7. Wall film thickness with the adapted dynamic boundary condition.

adapted dynamic boundary condition, the results in fig. 6 (right) already show a restriction for $x < 0.3\,\mathrm{m}$, so that two smaller rivulets enter the region with gas shear. Here, the rivulets are widened and forced to flow to the middle of the plate, where they form a unique rivulet again.

As shown in figs. 5 and 6, the adapted dynamic boundary condition is generally able to account for the contact line influence. In a more elaborate simulation, the adaption is tested for a complete wall film flowing down the inclined plate. The setup is still as mentioned above, except that instead of a single rivulet, a complete film with a total volume flow of $15.5 \cdot 10^{-6}\,\mathrm{m}^3/\mathrm{s}$ is initialised at the top of the plate and no gas shear stress is apparent. Figure 7 shows the result for the wall film with the contact line influence acting directly from the beginning. The initialised film starts to constrict immediately on both sides, and additionally, two stagnation points build up close to the middle of the film. Unfortunately, two small rivulets are starting to flow from the middle of the stagnation points, which physically should not happen, as the fluid there should be distributed to the sides. Further downstream these two rivulets join another one and in total four rivulets result from the initialised film. Nevertheless, further research of the model in these special cases is inevitable. Additionally, the simulated results will be compared to scheduled experimental investigations to validate the simulation and the adapted model.

The grid sensitivity of the rivulet width and shape is investigated as well with the test case of the inclined surface. For the sake of computational time, the physical domain is reduced to $0.3 \times 0.6\,\mathrm{m}^2$. The inclination and the contact angle are still 70° and the volume inflow is $1.8 \cdot 10^{-6}\,\mathrm{m}^3/\mathrm{s}$. The grid resolution varies from 25×50 cells up to 400×800 cells. This leads to grid cell lengths between $12 \cdot 10^{-3}$ and $0.75 \cdot 10^{-3}\,\mathrm{m}$. The rivulet width is evaluated in y-direction, perpendicular to the main flow direction. Within the calculation, the exact position of the three phase contact line in the outer cells of the rivulet is unknown. To calculate the physical rivulet width, only half of the outer cells is taken into account. This leads to an uncertainty of one cell length. Figure 8(a) shows the physical rivulet width over the running length for all resolutions. It has to be mentioned, that only every tenth data point is visualized with a marker to add clarity. Going from higher to lower resolution, two observations are apparent. First, a strong constriction towards a common mean value of about $7.3 \cdot 10^{-3}\,\mathrm{m}$ occurs at the top of the plate for the three higher resolutions. With increasing running length, the width oscillates around that value, with decreasing amplitudes for higher resolutions. The difference between the width is always below the above mentioned uncertainty of one cell

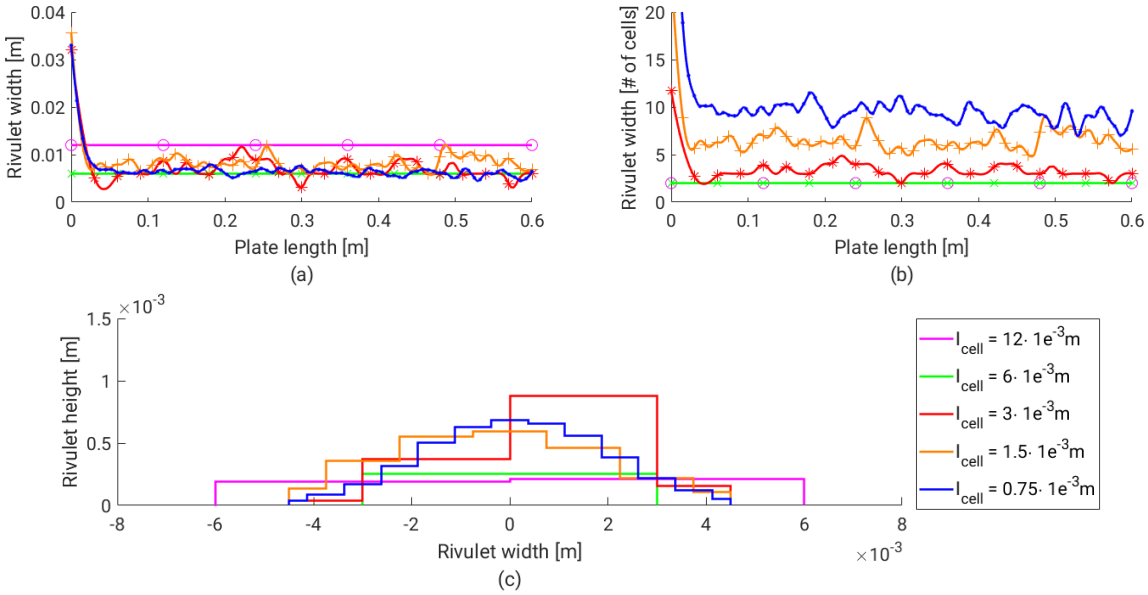

Figure 8. Rivulet width and mean cross section in flow direction depending on grid resolution.

length. The second observation is that for the two lower resolutions no change in width occurs over the whole running length. Although the results with $l_{cell} = 6 \cdot 10^{-3}\,\mathrm{m}$ lie in the same range as for higher resolutions, this is a sign for an underresolved simulation. This can also be seen in fig. 8(b), where the rivulet width is shown in number of cells. The underresolved simulations with $l_{cell} = 6 \cdot 10^{-3}\,\mathrm{m}$ and $l_{cell} = 12 \cdot 10^{-3}\,\mathrm{m}$ result in a constant width of two cells. Only for higher resolutions, an increase in number of cells is visible. The increase correlates to the resolution refinement, which indicates grid independency. Figure 8(c) shows the cross section of the rivulet averaged over the whole running length as a stairstep graph for better visualization of the rivulet height in each cell and the cell size itself. Again, the effect of the low resolution is visible, as the shape resembles a block profile instead of an arc. With increasing resolution, the shape develops to a more physical behaviour and the arc is resolved by more cells. Besides the rivulet width itself, also the shape and height tend to a common outcome for the three higher resolutions. The scheduled experimental validation, will give a better insight into which grid resolution will finally be needed.

As mentioned in the introduction, the motivation for the study is based on high-fogging in stationary gas turbines. Within this process, liquid films develop on the compressor blades and break up into separate rivulets. Neupert et al. [7] investigated this behaviour experimentally. Figure 9 shows a water film breakup on a blade's suction side in a staggered compressor cascade with flow from right to left. This case has been chosen as a reference case for the following simulation. The boundary conditions for the calculation of the wall film have been simulated by the authors in earlier publications [3], [11]. Figure 10 shows the shear stresses of the surrounding gas flow τ_{Gx} and the impacting droplets τ_{Ix}, as well as the gradient of the static pressure dp_{Gx} in the midsection plane of the blade's suction side. The amount of impacting droplets over the suction side of the blade is shown in fig. 11. It can be seen, that the droplets are only impacting onto the first 20% of the blade. The data fits the experimental setup as described in [7].

The result for the wall film height under the given conditions and the adapted dynamic boundary condition is shown in fig. 12. The wall film height is slowly increasing until about 30% chord length. The film seems to break up and rivulets are formed. However, they are not separated as clearly as the rivulets flowing down the inclined plate. The observed problem of liquid not being distributed sidewards at the stagnation point could cause the high number of rivulets. Again, further research is on the way to explore this problem and to extend the method. Nevertheless, the breakup position can be evaluated approximately. As can be seen, rivulets are built starting from a chord length of 30%. This generally agrees to the experimental data from [7], where the breakup occurs at about 25% chord length.

Conclusions

The present study focusses on the modelling of liquid rivulet flow and the transition from an intact liquid film to separate rivulets. The numerical description of a liquid film over a surface can be derivated from the Navier-Stokes equations and simplified in analogy to the lubrication theory. The consideration of rivulets is done by modifying the dynamic boundary conditions. A new term is introduced, that contributes to the force balance at the three phase contact line on the sides of a rivulet. Finally, simulation results were shown. Simple cases, such as single rivulet flow, but also more elaborate simulations, such as a liquid film flowing down an inclined plate and the flow over a compressor blade were performed. The results illustrate the general applicability of the proposed model adaption. It can be seen that the physical phenomena can be reproduced qualitatively. For a quantitative analysis, the model

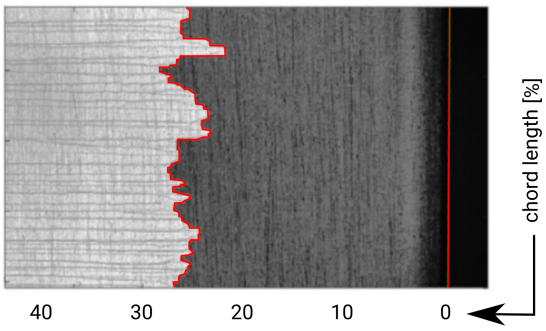

Figure 9. Processed image of water film breakup in a staggered compressor cascade [7].

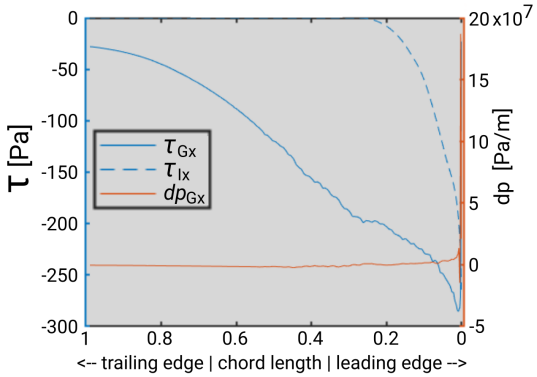

Figure 10. Boundary condition for the wall film simulation over a compressor blade.

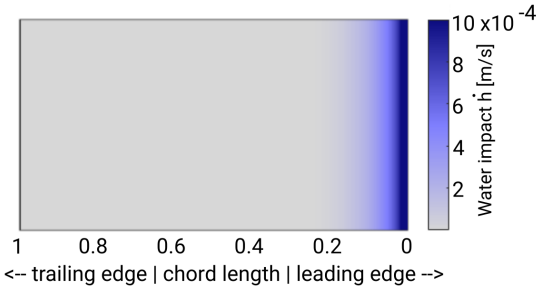

Figure 11. Impacting volume flow for the wall film simulation over a compressor blade.

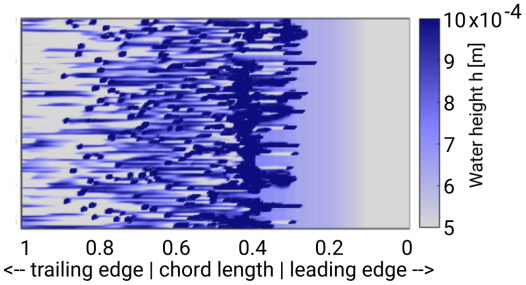

Figure 12. Wall film thickness on a compressor blade with the adapted dynamic boundary condition.

has to be extended to solve all the mentioned issues and in the end needs to be validated.

Acknowledgements

This project was supported by the German Research Foundation (DFG) (WE 2549/36-1). All authors of the paper kindly acknowledge the financial support of DFG for this project.

Nomenclature

d	diameter [m]
S	stagnation point
δ	thickness [m]
σ	surface tension [N/m]
θ	contact angle [°]
$\boldsymbol{u_{xy}}$	film velocity in x- and y-direction [m/s]
w	film velocity in normal direction [m/s]
$\dot{h}_I$	net volume source term per area [m/s]
h	wall film height [m]
x, y, n	wall film coordinates
ρ_L	liquid density [kg/m^3]
p	pressure [Pa]
μ_L	liquid dynamic viscosity [Pa s]
ϕ	potential [Pa]
g	gravity [m/s^2]
$\boldsymbol{\omega}$	rotation vector [rad/s]
$r_\perp$	orthogonal distance to $\boldsymbol{\omega}$ [m]
z	altitude [m]
t	time [s]
κ	curvature [1/m]
τ_G, τ_I	gas and impacting spray stress [Pa]
$\delta x, \delta y$	cell width [m]
l_{CL}	contact line length [m]
l_{cell}	grid cell length [m]
$\vec{n}_{CL}$	normal vector to contact line

T_σ force at stagnation point [N]
τ_{CL} stress term due to surface tension at contact line [Pa]

References

[1] K.M. Al-Khalil, T.G. Keith, and K.J. De Witt. Development of an Anti-Icing Runback Model. *28th Aerospace Sciences Meeting*, January 8-11, 1990.

[2] M.S. El-Genk and H.H. Saber. Minimum thickness of a flowing down liquid on a vertical surface. *Int. J. of Heat and Mass transfer*, 44:2809–2825, 2000.

[3] H. Gomaa. *Modeling of liquid dynamics in spray laden compressor flows*. PhD thesis, University of Stuttgart, Germany, 2014.

[4] H. Gomaa and B. Weigand. Modelling and investigation of the interaction between drops and blades in compressor cascades with a droplet laden flow. *ISROMAC-14*, February 27 - March 2, 2012.

[5] D.E. Hartley and W. Murgatroyd. Criteria for the break-up of thin liquid layers flowing isothermally over solid surfaces. *Int. J. of Heat and Mass transfer*, 7:1003–1015, 1964.

[6] M. Itoh and S. Matsuno. Scale effect on liquid flim formation in a prefilming type air-blast atomizer. *ILASS - Europe 2014*, September 8-10, 2014.

[7] N. Neupert, H. Gomaa, F. Joos, and B. Weigand. Investigation and modeling of two phase flow through a compressor stage: analysis of film breakup. *European J. of Mechanics B/Fluids*, 61:279–288, 2017.

[8] N. Neupert, J. Harbeck, and F. Joos. An experimentally derived model to predict the water film in a compressor cascade with droplet laden flow. *ASME Turbo Expo 2017: Turbomachinery Technical Conference and Exposition*, (GT2017-64121), June 26-30, 2017.

[9] O. Reynolds. On the theory of lubrication and its application to Mr. Beauchamp tower's experiments, including an experimental determination of the viscosity of olive oil. *Philisophical transactions of the royal society of London*, 177:157–234, 1886.

[10] A. Seck and B. Weigand. Evaporation modelling of water droplets in a transonic compressor cascade under fogging conditions. *ETC-13*, April 8-12, 2017.

[11] A. Seck, H. Gomaa, and B. Weigand. Improved modeling approach for the interaction between droplets and blades in a compressor cascade. *ISROMAC-17*, December 15-22, 2017.

[12] T. Young. An essay on the cohesion of fluids. *Philisophical transactions of the royal society of London*, 95: 65–87, 1805.

[13] K. Zhang. *An experimental study of wind-driven surface water transport process pertinent to aircraft icing*. PhD thesis, Iowa State University, USA, 2015.